How to cite: *Angew. Chem. Int. Ed.* **2022,** *61,* e202209289
International Edition: doi.org/10.1002/anie.202209289
German Edition: doi.org/10.1002/ange.202209289

VIP **Photo-Oxidation** *Very Important Paper*

Covalent-Bonding Oxidation Group and Titanium Cluster to Synthesize a Porous Crystalline Catalyst for Selective Photo-Oxidation Biomass Valorization

Jia-Nan Chang, Qi Li, Y. Yan, Jing-Wen Shi, Jie Zhou, Meng Lu, Mi Zhang, Hui-Min Ding, Yifa Chen, Shun-Li Li, and Ya-Qian Lan**

Abstract: The selective photo-oxidation of biomass-derived 5-hydroxymethylfurfural (HMF) to 2,5-furandicarboxylic acid (FDCA) is important due to its substitute-role in polyester-fabrication. Here, a titanium-cluster based metal-covalent organic framework nanosheet has been synthesized through the covalent-coupling between Ti_6-NH_2 and benzotrithiophene tricarbaldehyde (BTT). The integration of them endows the nanosheet with a visible-light-adsorption region, effective electron-hole separation-efficiency and suitable photo-oxidation ability. Specifically, its photo-selectivity for HMF-to-FDCA can be >95% with ≈100% conversion, which is more than 2, 5, and 10 times higher than MOF-901 (43%), Ti_6-NH_2 (19%) and under-darkness (9%), respectively. Notably, an O_2-based mechanism is proposed and the vital roles of Ti_6-NH_2 and BTT are verified by DFT calculations. This work might facilitate the exploration of porous-crystalline-catalysts for selective biomass-valorization.

Introduction

With the increasing need for fuel and energy supply, the exploration of renewable carbon feedstocks (e.g., biomass) has recently attracted tremendous attention due to their potential in substituting the petroleum resources to generate value-added fuels or fine chemicals.[1] The efficient valorization of biomass could play a role in solving energy and environmental problems for future sustainable development.[2] For example, 5-hydroxymethylfurfural (HMF), the dehydration product of C6 carbohydrates, is a vital platform chemical for biomass-derived intermediates, which has been utilized for the syntheses of a series of pharmaceuticals, monomers and fine chemicals (e.g., maleic anhydride (MA), 2,5-diformylfuran (DFF), 5-hydroxymethyl-2-furancarboxylic acid (HMFCA), and 2,5-furandicarboxylic acid (FDCA), etc.).[3] Among them, FDCA is identified by the department of energy (U.S.A) to be a key bio-derived chemical and most importantly, a vital monomer for the synthesis of bio-based polyethylene furandicarboxylate (PEF) that has much potential to replace commonly applied polyethylene terephthalate (PET).[4] In this regard, it is particularly important to obtain FDCA through the highly selective oxidation of HMF and techniques including traditional thermal catalysis, electro- or photo-catalysis have been studied.[5] Compared with others, photo-catalysis driven by light and O_2 has attracted enormous attention in promoting photo-oxidation of HMF due to its advantages of cost-effectiveness and sustainability, consistent with the concept of sustainable development strategy.[6] However, the photo-oxidation products of HMF are diversified (including DFF, HMFCA or FFCA in addition to FDCA) and the relative mechanisms are complicated to be investigated, which makes it a giant challenge to achieve highly selective photo-oxidation of HMF-to-FDCA especially that conditions using visible light and molecular O_2.[7] Henceforth, the quest for cost-effective, stable, visible-light responsive and highly selective photo-catalysts is highly pursued for the photo-oxidation of HMF-to-FDCA.

The accomplishment of highly selective photo-oxidation of HMF-to-FDCA lies in the suitably tuned photo-oxidation ability of photo-catalysts. Thus, photocatalysts should have appropriate energy band structures and light absorption region, which can effectively use electrons and holes generated by light as well as to avoid insufficient oxidation capacity or peroxidation. At present, TiO_2 or its derivatives are the most widely used catalysts in the photo-oxidation of biomass, ascribed to their chemical/thermal stability, low cost and toxicity, and resistance to photo-corrosion, etc.[8] However, their applications in HMF photo-oxidation still face drawbacks like: i) TiO_2 has wide band gap (3.2 eV) and requires UV light (<5% of solar radiation) for photo-activation;[9] ii) the photocatalytic system of TiO_2 generally forms highly active oxidative species (e.g., hydroxyl radicals) with over-oxidation ability that would destroy the furan ring of HMF and is considered to be unselective for the HMF oxidation[3c] and iii) most of them are in nonporous solid-

[*] Dr. J.-N. Chang, Q. Li, J.-W. Shi, H.-M. Ding
Jiangsu Collaborative Innovation Centre of Biomedical Functional Materials, Jiangsu Key Laboratory of New Power Batteries, School of Chemistry and Materials Science, Nanjing Normal University
Nanjing 210023 (P. R. China)
Dr. Y. Yan, J. Zhou, M. Lu, M. Zhang, Prof. Y. Chen, Prof. S.-L. Li, Prof. Y.-Q. Lan
School of Chemistry, South China Normal University
Guangzhou, 510006 (P. R. China)
E-mail: chyf927821@163.com
yqlan@njnu.edu.cn
yqlan@m.scnu.edu.cn

particle forms, resulting in less-exposed catalytic sites and are not conducive to substrate adsorption or mass transfer. Despite some pioneering strategies including metal/non-metal doping,[10] coupling dyes/narrow band gap semiconductors,[11] and ligand-to-metal charge transfer (LMCT) interaction,[12] etc have been proposed, most of them are still challenging in designing well-defined structures with suitable band gaps, visible-light absorption region and appropriate photo-oxidation ability that enable the highly selective photo-oxidation of HMF-to-FDCA. Similar problems have also been existed for other photocatalysts, such as porous polymers (e.g., CTF Th@SBA-1),[5b] semiconductors (e.g., Nb_2O_5-800, $MAPbBr_3$, and CdS, etc.) or molecular catalysts (e.g., CoPz/g-C_3N_4),[13] etc. Therefore, it would be much necessary to develop powerful photocatalysts that can accurately regulate the energy band structures and light-absorption region to meet the stringent requirements for highly selective photo-oxidation HMF-to-FDCA.

Metal–organic frameworks (MOFs), arising as typical porous crystalline materials constructing from metal ions/clusters and organic linkers, are well-known to have unique properties of well-defined structures, high surface area, functional and structural tunability, etc.[14] Specifically, Ti-based MOFs have been explored in many photocatalytic applications such as CO_2 reduction, CO_2 cycloaddition to epoxides, or hydrogen evolution, etc.[15] In comparison to TiO_2, the assembly of Ti ions/clusters and organic ligands might generate efficient LMCT interaction to tune the inert property of Ti-based MOFs, in which they would possess uniformly-dispersed Ti ions/clusters, high porosity and well-defined structures that have much potential in the photo-oxidation of HMF-to-FDCA.[16] However, the applications of Ti-based MOFs in HMF photo-oxidation are still rare as far as we known. To this end, we intend to covalently connect the amino functionalized titanium cluster (Ti_6-NH_2) with oxidation group to obtain Ti-cluster based metal-covalent organic framework. The following considerations are listed as follows: i) Ti_6-NH_2 has similar energy band structures as that of TiO_2 and can be covalently connected with oxidation groups through stable Schiff-base condensation interaction to efficient tune the band gaps and light-absorption properties;[17] ii) the addition of oxidation group can effectively adjust its optical band gap, improve its utilization of electrons and holes, and promote the formation of active intermediates of HMF and iii) the effective connection between Ti_6-NH_2 and oxidation group through covalent connection might provide high stability and promote the light-driven LMCT to facilitate electron-hole separation/transfer for highly selective photo-oxidation HMF-to-FDCA.[18] Besides, traditional Ti-MOFs are generally hard to crystallize and still short in stability due to their inherent relatively weak coordination bonding. We deduce that thus-designed Ti-cluster based metal-covalent organic framework with strong covalent bonding might probably be potential candidates to improve the efficiency of photo-oxidation HMF-to-FDCA, while the syntheses of such interesting structures are still rare and challenging to the best of our knowledge.

Herein, we have prepared a kind of Ti-cluster based metal-covalent organic framework (denoted as MCOF-Ti_6BTT) nanosheets by the covalent connection of Ti_6-NH_2 and BTT, and successfully applied it in highly selective photo-oxidation of HMF-to-FDCA (Scheme 1). The covalent connection between light-absorption group (Ti_6-NH_2) and oxidation group (BTT) enables the visible-light driven electron-hole to efficiently separate and transfer from BTT to Ti_6-NH_2 moiety, resulting in the photoexcited electrons (on Ti_6-NH_2) and holes (on BTT) that can be used for O_2 activation and HMF oxidation reactions, respectively. Notably, its photo-selectivity for HMF-to-FDCA can reach up to $>95\,\%$ with approximately $100\,\%$ conversion under visible light, which is more than 2, 5, and 10 times higher than MOF-901 ($43\,\%$), Ti_6-NH_2 ($19\,\%$) and under-darkness ($9\,\%$), respectively. The high performance makes it to be one of the best HMF-to-FDCA photo-catalysts reported to date. Based on the experimental results and density functional theory (DFT) calculations, we illustrate the possible mechanism, in which O_2 with energy-level between Ti_6-NH_2 (LUMO) and BTT (HOMO) gets electrons during the LMCT process to generate superoxide-radicals ($^{\bullet}O_2^-$, and $^1O_2$), meanwhile HMF uses the timely generated holes to form active-intermediates. Afterwards, the superoxide-radicals and active-intermediates are joined to obtain the key-intermediates and further selectively produce FDCA on MCOF-Ti_6BTT. This work sheds fresh light on the exploration of porous crystalline catalyst in highly selective photo-oxidation of HMF-to-FDCA.

Results and Discussion

MCOF-Ti_6BTT was synthesized through the Schiff-base condensation reaction of Ti_6-NH_2 and BTT and a kind of yellow powder was obtained after 72 h at 100 °C (Figure 1a, detail see Supporting Information). To define the crystalline structure of MCOF-Ti_6BTT, the powder X-ray diffraction (PXRD) combined with theoretical structural simulations were performed. A hexagonal $P6_3$ space group based on MCOF-Ti_6BTT was set up based on the basic evaluation of the structure, which was then defined by Pawley refinements of the PXRD patterns for full profile fitting of the proposed

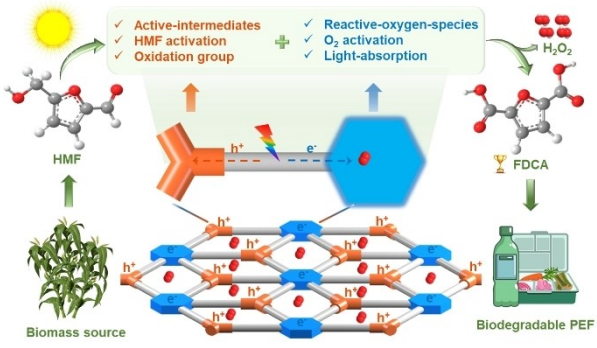

Scheme 1. Schematic representation of Ti-cluster based metal-covalent organic framework for selective photo-oxidation of HMF-to-FDCA.

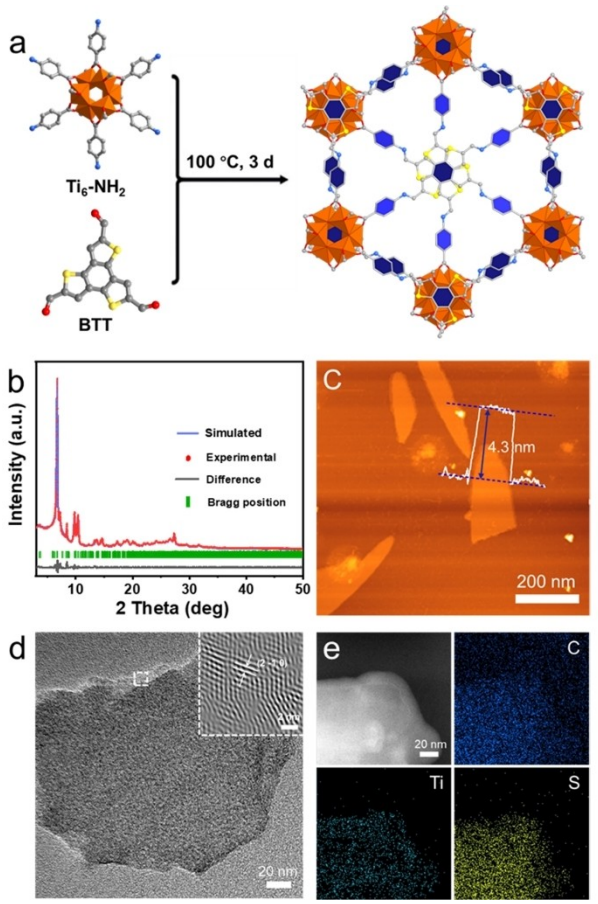

Figure 1. Structure and characterization of MCOF-Ti_6BTT. a) Schematic representation of the synthesis of MCOF-Ti_6BTT through the condensation of Ti_6-NH_2 and BTT. b) Experimental (red dot) and simulated (blue line) PXRD patterns of MCOF-Ti_6BTT. c) Atomic Force Microscope (AFM) image and height profile of MCOF-Ti_6BTT. d) HRTEM image and lattice fringes. e) STEM and elemental mapping images of MCOF-Ti_6BTT.

models (Table S1). Based on the simulations, it possesses a unit cell parameter ($a=27.1778$ Å, $b=27.1778$ Å, and $c=14.4463$ Å, $\alpha=\beta=90°$, $\gamma=120°$) that complies with the hypothesis. Moreover, the simulated PXRD pattern using AB stacking mode reproduced the experimentally observed curve while AA stacking did not, which was supported by the difference plot with unweighted-profile R factor (R_p) of 3.41 % and weighted profile R factor (R_{wp}) of 4.55 % (Figure 1b, details see Supporting Information). In the PXRD pattern, it has observed peaks at 3.75°, 6.50°, 7.20°, and 12.27°, which can be assigned to the (1 0 0), (2 -1 0), (1 0 1) and (0 0 2) facets of MCOF-Ti_6BTT, respectively. Besides, MCOF-Ti_6BTT possesses 2D sheet stacked structure and the distance between adjacent sheets is 14.45 Å (Figure 1a), suggesting the possibility in generating 2D nanostructures like nanosheets. In the Fourier-transform infrared spectroscopy (FT-IR) measurements, the C=N stretching vibration band at 1625 cm^{-1} appeared in the resultant MCOF-Ti_6BTT (Figure S1). Meanwhile, the C=O stretching vibration band (1700 cm^{-1}) and -NH_2 vibration band (3200–3500 cm^{-1}) belonging to the relative reactant monomers decrease obviously in MCOF-Ti_6BTT, implying the successful generation of covalent bond and might permit high stability for MCOF-Ti_6BTT.[19]

To investigate the chemical states of the existed elements in MCOF-Ti_6BTT, X-ray photoelectron spectroscopy (XPS) measurements have been conducted. For the XPS spectra of MCOF-Ti_6BTT, five main peaks with binding energy of 458.00 164.16, 284.54, 398.36 and 531.69 eV are ascribed to Ti 2p, S 2p, C 1s, N 1s and O 1s, respectively (Figure S3). In the S 2p region, two kinds of peaks with binding energies of 164.07 eV (S $2p_{3/2}$) and 165.29 eV (S $2p_{1/2}$) can be attributed to the characteristic peaks of sulfur (C–S) in BTT unit (Figure S6). Besides, Ti $2p_{3/2}$ (458.7 eV) and Ti $2p_{1/2}$ (464.2 eV) spin orbits are also observed, suggesting the tetravalent valance of Ti in MCOF-Ti_6BTT (Figure S5).[20]

Besides, we have conducted the atomic force microscope (AFM) tests to evaluate the thickness and morphology of MCOF-Ti_6BTT. In the AFM image, MCOF-Ti_6BTT shows nanosheet morphology (size, ≈200 nm) and the thickness was calculated to be ≈4.3 nm in the height profile (Figure 1c). In addition, the morphology detected in AFM tests was further confirmed by the TEM test (Figure 1d). Specifically, the oriented lattice fringes could be observed in the high-resolution TEM (HR-TEM) image and the lattice spacing of 1.23 nm is assigned to the (2 -1 0) plane, confirming the high crystallinity of the obtained MCOF-Ti_6BTT nanosheets (inset image, Figure 1d). Additionally, elemental mapping analysis reveals that C, N, S, and Ti are uniformly distributed in MCOF-Ti_6BTT nanosheets (Figure 1e). Thus, MCOF-Ti_6BTT with nanosheet morphology is obtained based on above characterizations, which would be much beneficial for the accessibility of active sites and mass transfer in photo-catalytic reactions.

In general, chemical stability is a vital factor to evaluate the basic property of MCOF-Ti_6BTT. It was examined through the immersing of MCOF-Ti_6BTT in different solvents (i.e. N, N-dimethylformamide, acetonitrile, methanol and H_2O) for more than 5 days. After tests, the samples were characterized by the PXRD and FTIR tests, and the results showed that it could remain the structure integrity when compared with the state before tests, implying the high chemical stability of the covalent-bonding structure as mentioned above (Figure S7, S8).

Furthermore, UV/Vis diffuse reflectance spectroscopy (DRS) and ultraviolet photoelectron spectroscopy (UPS) were carried out to determine the basic optical properties of MCOF-Ti_6BTT (Figure S9). It exhibits a broad visible-light absorption range (i.e. 300 to 700 nm), and the corresponding band gap (E_g) is determined to be 2.35 eV for MCOF-Ti_6BTT by the Tauc plots (Figure S9). The highest unoccupied molecular orbital (HOMO) of MCOF-Ti_6BTT is calculated to be −6.37 eV (vs. E_v) from the UPS tests and the related lowest unoccupied molecular orbital (LUMO) is thus to be −4.02 eV (vs. E_v). Mott–Schottky measurements were further conducted to determine the band positions of MCOF-Ti_6BTT and the results were consistent with those from the UPS tests (Figure 2d and Figure S9). In previous literatures, the results have revealed that the photo-

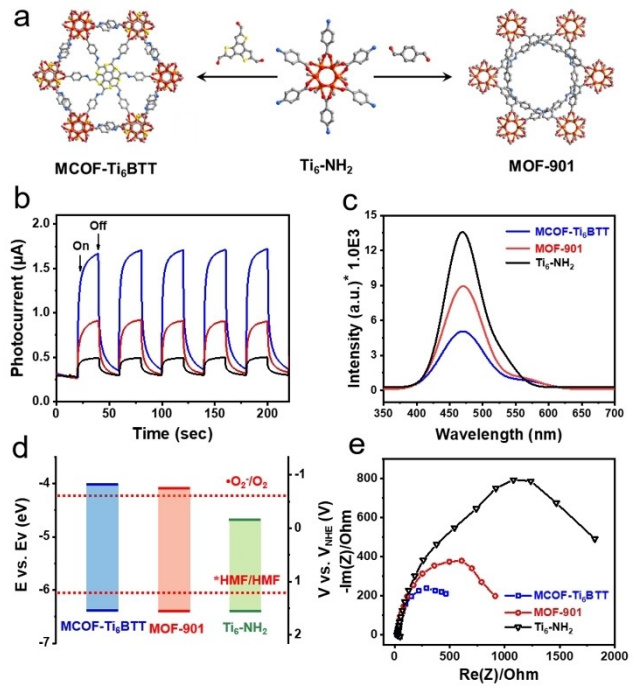

Figure 2. Characterizations of the optical properties for MCOF-Ti_6BTT, MOF-901 and Ti_6-NH_2. a) The structural diagram of MCOF-Ti_6BTT, MOF-901 and Ti_6-NH_2. b) Transient photocurrent response of MCOF-Ti_6BTT (blue), MOF-901 (red) and Ti_6-NH_2 (black). c) PL of MCOF-Ti_6BTT, MOF-901 and Ti_6-NH_2. d) Band-structure diagram for MCOF-Ti_6BTT, MOF-901 and Ti_6-NH_2. e) Nyquist plots of MCOF-Ti_6BTT, MOF-901 and Ti_6-NH_2.

oxidation of HMF could generate reactive-oxygen-species (ROS) such as superoxide ($^{\bullet}O_2^-$) or singlet oxygen ($^1O_2$). Typically, the photocatalyst is required to have a more negative LUMO potential than the O_2 reduction potential (e.g., $O_2/^{\bullet}O_2^-$, theoretically −0.62 V vs. NHE, pH 7 and −4.22 eV vs. E_v, vacuum level) as well as more positive HOMO potential than the HMF oxidation potential (theoretically 1.23 V vs. NHE, pH 7 and −6.09 eV vs. E_v). In this work, the HOMO and LUMO of MCOF-Ti_6BTT match well with the band gap of O_2 activation.[21] MOF-901 and Ti_6-NH_2 were also tested by DRS, UPS and Mott–Schottky (Figure S10, S11).

As comparison, MOF-901, composed of Ti_6-NH_2 and 1,4-phthalaldehyde, was also synthesized according to the reported literature and compared with MCOF-Ti_6BTT (Figure 2a). The intensity of transient photocurrent response of MCOF-Ti_6BTT shows much higher than MOF-901 and Ti_6-NH_2, which suggested that that the covalent connection between Ti_6-NH_2 and BTT in MCOF-Ti_6BTT can lead to higher photoinduced electron separation and transport efficiency (Figure 2b). Additionally, photoluminescence (PL) was conducted to investigate the charge separation behaviors. The PL intensity of MCOF-Ti_6BTT is significantly quenched compared to Ti_6-NH_2 and BTT (Figure 2c). These results show that the covalent connection between Ti_6-NH_2 and BTT can effectively enhanced electron-hole separation and prevent recombination, resulting from the efficient electron transfer efficiency that might be achieved by the LMCT effect in MCOF-Ti_6BTT. The electrochemical impedance spectroscopy (EIS) was also conducted to investigate the charge transfer resistance (Figure 2e). The Nyquist plots demonstrated that MCOF-Ti_6BTT has much smaller charge transfer resistance than MOF-901 and Ti_6-NH_2 due to its smallest semicircle in the high frequency region. The results suggest that MCOF-Ti_6BTT has stronger charge transfer ability and also imply the vital role of BTT in enhancing the LMCT effect. Therefore, we have obtained a kind of MCOF-Ti_6BTT nanosheets with visible-light absorption region, high stability and effective electron-hole separation/transfer ability, which has much potential to be applied in selective photo-oxidation of HMF.

The photo-oxidation property of HMF was evaluated in a photo-catalysis system, in which visible light (400–800 nm) was applied and the tests were conducted under O_2 atmosphere (Figure S23, details see Supporting Information). Table S2 shows the results of exploratory experiments of the photo-oxidation of HMF-to-FDCA with different materials as the photocatalysts. Control experiments were firstly conducted to gain insight into the photocatalytic process. Firstly, the stability of HMF and FDCA under the reaction conditions was studied. The photolytic decomposition of HMF without MCOF-Ti_6BTT was negligible (0.1 %) after 36 h under the reaction conditions, and no photolytic decomposition of FDCA was observed either (Table S2). In the presence of MCOF-Ti_6BTT, the conversion and selectivity of HMF-to-FDCA gradually increased with the increase of reaction time (6 to 36 h) and finally reached to 99 % and 95 %, respectively (Figure 3a and Figure S24–27). The result achieved was represented to be one of the best Ti-based materials to date (Table S3). Meanwhile, DFF and FFCA gradually disappeared during the time-interval reaction process (Figure 3a). In order to gain insight into the possible reaction process, and reveal the specific effects of electron-hole pairs and ROS (e.g., $^{\bullet}O_2^-$ and $^1O_2$) produced in the photocatalytic process, we have conducted a series of control experiments with the addition of different specific radical scavengers (Figure 3b). When p-benzoquinone (BQ) was presented as the superoxide radical scavenger, the conversion efficiency was low (23 %). Meanwhile, when isopropanol (IPA) was added as the hydroxyl scavenger and potassium iodide (KI) as the hole scavenger, the conversion rates were 95 % and 41 %, respectively. Thus, it can be seen that the reactive oxygen species (i.e. $^{\bullet}O_2^-$ and $^1O_2$) and photogenerated holes are indeed involved in the photo-oxidation of HMF.

To unveil the transformation process of HMF under photocatalytic conditions, we have performed the in situ diffuse reflectance infrared Fourier transform spectroscopy (DRIFTs) measurements (Figure 3f). After the system was equilibrated, vibrations corresponding to C–OH (1054 cm^{-1}), O–H (1351 cm^{-1}), O–O (1152 cm^{-1}), and C=N (1605 cm^{-1}) for MCOF-Ti_6BTT were apparent. Upon visible light irradiation, the peak intensity belonging to the vibrational modes of C=O group (1760 cm^{-1}) for FDCA enhances significantly, while the intensity of peak signals at 1730 cm^{-1} belonging to the vibrational mode of the C=O group for

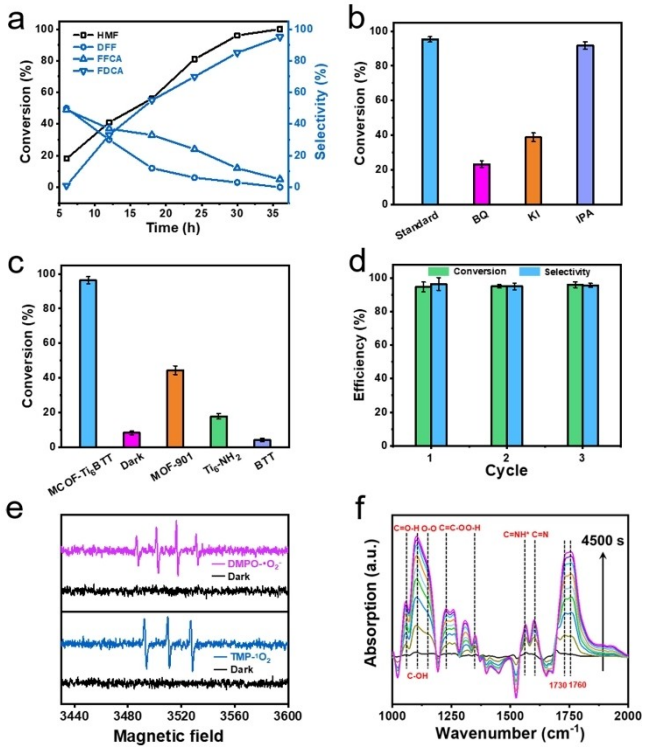

Figure 3. Photo-catalytic performances of MCOF-Ti_6BTT, MOF-901, Ti_6-NH_2 and BTT in photo-oxidation of HMF-to-FDCA. a) Time-dependent conversion and selectivity efficiency of HMF, DFF, FFCA and FDCA for MCOF-Ti_6BTT. b) Conversion efficiency of various scavengers for photo-oxidation of HMF-to-FDCA. c) Photo-catalytic performances of MCOF-Ti_6BTT and contrast samples. d) Cycling performance of MCOF-Ti_6BTT. e) EPR signals of the reaction solution under the dark and full spectrum light illumination in the presence of TMP and DMPO as the spin-trapping reagents. f) DRIFTs spectra of HMF transformation during the photo-oxidation of HMF-to-FDCA by MCOF-Ti_6BTT.

DFF firstly increases and then decreased obviously,[22] indicating that HMF is firstly transformed into DFF and finally into FDCA during the photocatalytic process (Figure 3f). The result shows that DFF is the key intermediate during the photocatalytic process, which matches well with the above-mentioned time-interval reaction results.

We also tested the photo-oxidation of HMF for different contrast samples (e.g., MOF-901, BTT and Ti_6-NH_2) to reveal the superiority of MCOF-Ti_6BTT. The conversion efficiency of MOF-901 for photocatalytic oxidation of HMF is 43 %, much lower than that of MCOF-Ti_6BTT (Figure 3c). In addition, the HMF conversion efficiency of Ti_6-NH_2 and BTT are only 19 % and <10 %, respectively. Based on the above results, it can be seen that the covalent connection of Ti_6-NH_2 and BTT would generate efficient light-driven LMCT to facilitate the electron-hole separation/transfer to improve the photo-oxidation performance of HMF-to-FDCA. Besides, the cycling stability is also a vital factor to evaluate the durability of the photocatalyst.[5b] Thus, we have carried out the cycling tests. After three cycling experiments, the catalytic performance remains almost unchanged, proving the high cycling stability of MCOF-Ti_6BTT (Figure 3d). Furthermore, the structural integrity of MCOF-Ti_6BTT was retained after the cycling tests as confirmed by the PXRD and FTIR characterizations (Figure S12, S13).

Based on the excellent performance of MCOF-Ti_6BTT, we further gain insight into the detailed reaction process of the highly selective photo-oxidation HMF-to-FDCA, during which various contrast experiments and characterizations have been conducted. Specifically, HMF did not transform under N_2 atmosphere, and the conversion rate under air was only 28 %, indicating that O_2 was the oxidant for the selective photo-oxidation of HMF-to-FDCA (Table S4). Furthermore, the reactive oxygen species (e.g., $^1O_2$ and $^\bullet O_2^-$) were detected and spin-trapped by electron paramagnetic resonance (EPR) measurements. When using 2,2,6,6-tetramethylpiperidine (TMP) as the spin-trapping reagent, a characteristic 1:1:1 triplet EPR signal ($g=2.0019$) is detected, which is assigned to the signal of TMP-$^1O_2$ produced through the reaction of $^1O_2$ and TMP (Figure 3e). Moreover, the formation of superoxide $^\bullet O_2^-$ has also been confirmed using 5,5-dimethyl-1-pyrroline N-oxide (DMPO) as the spin-trapping agent, in which a characteristic EPR signal of DMPO-$^\bullet O_2^-$ ($g=2.0017$) has also been detected in the EPR tests. It is noted that no characteristic EPR signal was detected in both situations without illumination. Based on the above analyses, we can conclude that the selective photo-oxidation of HMF in the present system is achieved through the combined contribution from atmospheric O_2, photogenerated electrons (e^-), holes (h^+), $^\bullet O_2^-$, and $^1O_2$ species. During these reaction process, H_2O_2 as the the important side product might be produced.[24] In order to confirm our hypothesis, we tested the photocatalytic reaction solution by iodometry and H_2O_2 could indeed be detected (Figure S22).

DFT calculations are applied to understand the photo-excitation process and catalytic reaction mechanisms. We firstly adopt finite cluster calculations for the MCOF-Ti_6BTT to reduce the computation time effectively, as we assume the long rang interaction in a periodic order is trivial. Theoretical simulation UV/Vis DRS of MCOF-Ti_6BTT is shown in Figure S18. It can be noted that the first peak originates from the transition from HOMO to LUMO, thus the ICT process can be readily occurred by light irradiation, which further forms photogenerated electrons located on Ti-centers and photogenerated holes centered at BTT unit. The light-absorption of MCOF-Ti_6BTT in the visible-light region might be attributed to the effective charge transfer from the BTT ligand to Ti_6-NH_2, thus promoting the photocatalytic reactions. To obtain a more straightforward insight into the photogenerated electron dynamic processes, the state populations of photogenerated carries are calculated using time-dependent ab initio non-adiabatic molecular dynamics (NAMD) simulations. We initiate the NAMD calculations with a photogenerated electron localized in the LUMO of MCOF-Ti_6BTT. Figure 4a presents the evolution of populations for the ground state (GS), the excited state (ES) and O-state involved in the electron-hole recombination dynamics. The time scale shown is MCOF-Ti_6BTT obtained by exponential fitting of the data. After ≈ 0.4 ps, around 20 % of the electron

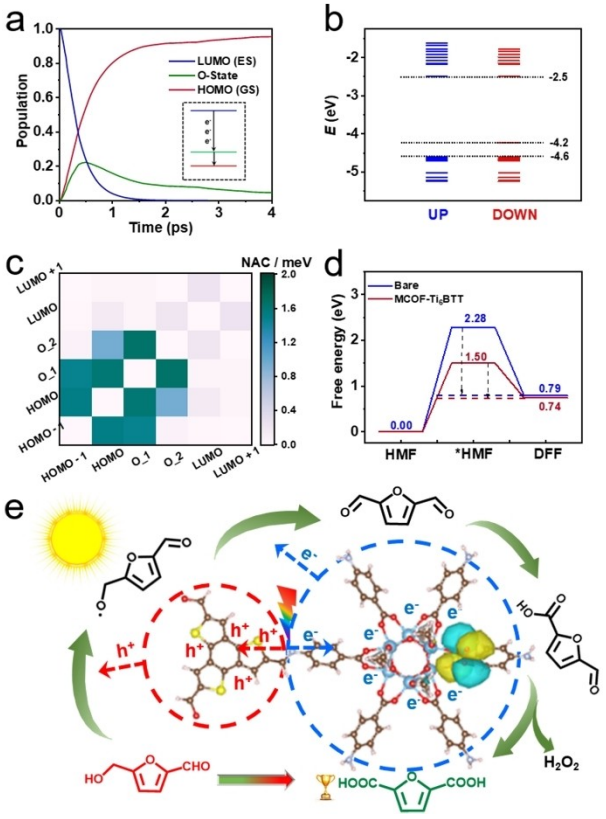

Figure 4. DFT calculations and the proposed reaction mechanism. a) Charge carriers trapping and recombination dynamics of MCOF-Ti_6BTT. b) Electronics structure diagram of MCOF-Ti_6BTT. c) Averaged absolute values of NAC between energy levels. d) Free energy diagrams of the photo-oxidation of HMF-to-DFF through the $^{\bullet}O_2^-$ pathway (bare stands for without catalyst). e) Schematic diagram of the photo-oxidation of HMF-to-FDCA through the $^{\bullet}O_2^-$ pathway.

transfers to O_2 and ≈10 % electrons can be stabilized on O_2 for more than 2 ps. Moreover, we can see that it's a nice bridge through the O_2 level. Electrons will be coupled with the energy level of O_2 in the process from LUMO to HOMO, resulting in electron transfer and the formation of $^{\bullet}O_2^-$. Besides, we present the fluctuations of electronic orbital energies along time evolution of trapping states originating from the atomic motions to understand the electron-phonon (e-p) coupling (Figure S19). The result shows that although the energy level of O_2 is close to HOMO with the change of time, it can still remain stable between the band gaps of MCOF-Ti_6BTT, which implies the strong coupling between O_2 and MCOF-Ti_6BTT.

In addition, to understand the interaction between HOMO, LUMO and O_2 level, we present the electronic structure diagram of MCOF-Ti_6BTT (Figure 4b). It can be seen that in the process of electron transfer, the oxygen level is between BTT donor (HOMO, 4.6 eV) and Ti_6-NH_2 receptor (LUMO, 2.5 eV). The calculation results show that because the O_2 level is located in the band gap of MCOF-Ti_6BTT, there is a certain possibility of carrier transfer to O_2. The underlying physics of the photogenerated electron dynamics can be further illustrated by the averaged non-adiabatic coupling (NAC) element between different states. As a result, the NAC between the neighboring states is clearly larger than that of the separated states (Figure 4c). Namely it is much easier for the photogenerated electrons to hop between the neighboring states. Besides, the NAC of e-h recombination is smaller than that of charge transfer from MCOF-Ti_6BTT to O_2, further verifying the formation of $^{\bullet}O_2^-$ (Figure 4c).

After the successful photo-oxidation of O_2, the following catalytic reaction mechanism of MCOF-Ti_6BTT in highly selective photo-oxidation HMF was studied by the free energy calculation. The photo-oxidation of HMF-to-FDCA may produce two vital intermediates (i.e. DFF and HMFCA) and have two related pathways. In this work, we find that DFF is the key intermediate rather than HMFCA in the process of HMF-to-FDCA. To gain more insight into the detailed photo-catalytic process, we calculate the photo-catalytic pathways for both $^1O_2$ and $^{\bullet}O_2^-$. Previous literatures have proved that $^1O_2$ participates in the HMF oxidation spontaneously, which can be photo-generated through the intersystem crossing (ISC) and inserted into the C–H bond (alcohol function group) of HMF to generate following intermediates.[5b,13d] Generally, $^1O_2$ can also participate in the catalytic process as an active species and it can be generated through the energy transfer from the excited photocatalyst to molecular O_2 or the hole (h^+) oxidation of $^{\bullet}O_2^-$ during the light excitation process. Reaction mechanism of photo-oxidation of HMF by $^1O_2$ has been studied by the free energy calculation, which matches well with the reported literatures (Figure S20, S21).[13d,23] As for the reaction mechanism of $^1O_2$ participated HMF photo-oxidation process is relatively independent and clear, and some literatures have also conducted sufficient investigations, we will mainly focus on $^{\bullet}O_2^-$. Therefore, we have calculated the $^{\bullet}O_2^-$ participated process for the HMF conversion to the vital intermediate (i.e. DFF). The conversion from HMF to DFF requires two dehydrogenation processes, from HMF to *HMF and further to DFF (Figure S24–S27). The first process is the rate determining step (RDS). As shown in Figure 4d, the energy barrier of HMF conversion to *HMF in the presence of MCOF-Ti_6BTT is preferred than that without catalyst. Compared with the high energy barrier of 2.28 eV (without MCOF-Ti_6BTT), it is only 1.5 eV for MCOF-Ti_6BTT, which indicates that the adsorption and activation of HMF are more favorable in presence of MCOF-Ti_6BTT (Figure 4d). Based on the above experiments and analysis, a possible mechanism is proposed to illustrate the photo-oxidation of HMF by MCOF-Ti_6BTT: driven by visible-light irradiation, the PET process takes place from BTT (HOMO) to Ti_6-NH_2 (LUMO) after absorbing photons; then O_2 with energy-level between Ti_6-NH_2 (LUMO) and BTT (HOMO) gets electrons to generate superoxide-radicals (i.e. $^{\bullet}O_2^-$, and $^1O_2$), meanwhile HMF uses the timely generated holes to form active-intermediates; afterwards, the superoxide-radicals and active-intermediates are joined to obtain the key-intermediates, followed by the subsequent process to selectively produce FDCA on MCOF-Ti_6BTT (Figure 4e and Figure S21).

Conclusion

In summary, we have prepared a case of Ti-cluster based metal-covalent organic framework nanosheet (≈4 nm) by the covalent-coupling between Ti_6-NH_2 (light-absorption unit) and benzotrithiophene tricarbaldehyde (BTT, oxidation unit). The covalent connection between Ti_6-NH_2 and BTT facilitates the visible-light driven electron-hole separation and transfer from BTT to Ti_6-NH_2 moiety, resulting in the photoexcited electrons (on Ti_6-NH_2) and holes (on BTT) that can be used for O_2 activation and HMF oxidation reactions, respectively. Noteworthy, its photo-selectivity for HMF-to-FDCA can reach up to >95 % with approximately 100 % conversion under visible light, which is more than 2, 5, and 10 times higher than MOF-901 (43 %), Ti_6-NH_2 (19 %) and under-darkness (9 %), respectively. Based on a series of comparative experiments, characterizations (e.g., EPR, DRIFTs, Mott–Schottky, UPS), and DFT calculations (e.g., finite cluster calculations, electronic structure diagram and NAC, etc.), we illustrate an O_2-involved mechanism, in which photo-excited electrons (on Ti_6-NH_2) and holes (on BTT) are applied for O_2 and HMF activation to form reactive-oxygen-species and active intermediates, respectively, followed by their joined reaction to obtain key-intermediates and further selective produce FDCA. This work would provide a new insight into the design of porous crystalline photocatalysts for the highly selective biomass valorization.

Acknowledgements

This work was financially supported by the NSFC (Grants 21871141, 21871142, 21901122, 22071109, 22105080, 22171139 and 92061101), the Excellent Youth Foundation of Jiangsu Natural Science Foundation (No. BK20211593), Priority Academic Program Development of Jiangsu Higher Education Institutions and the Foundation of Jiangsu Collaborative Innovation Center of Biomedical Functional Materials.

Conflict of Interest

The authors declare no conflict of interest.

Data Availability Statement

The data that support the findings of this study are available from the corresponding author upon reasonable request.

Keywords: 2,5-Furandicarboxylic Acid · 5-Hydroxymethylfurfural · Biomass · Covalent Organic Framework · Photocatalysis

[1] a) D. Esposito, M. Antonietti, *Chem. Soc. Rev.* **2015**, *44*, 5821–5835; b) A. J. Ragauskas, C. K. Williams, B. H. Davison, G. Britovsek, J. Cairney, C. A. Eckert, W. J. Frederick, J. P. Hallett, D. J. Leak, C. L. Liotta, J. R. Mielenz, R. Murphy, R. Templer, T. Tschaplinski, *Science* **2006**, *311*, 484–489.

[2] a) Z. Zong, S. Mazurkewich, C. S. Pereira, H. Fu, W. Cai, X. Shao, M. S. Skaf, J. Larsbrink, L. Lo Leggio, *Nat. Commun.* **2022**, *13*, 1449; b) H. Wu, H. Li, Z. Fang, *Green Chem.* **2021**, *23*, 6675–6697.

[3] a) C. Li, J. Li, L. Qin, P. Yang, D. G. Vlachos, *ACS Catal.* **2021**, *11*, 11336–11359; b) C. Xu, E. Paone, D. Rodríguez-Padrón, R. Luque, F. Mauriello, *Chem. Soc. Rev.* **2020**, *49*, 4273–4306; c) H. G. Cha, K.-S. Choi, *Nat. Chem.* **2015**, *7*, 328–333; d) T. Xia, W. Gong, Y. Chen, M. Duan, J. Ma, X. Cui, Y. Dai, C. Gao, Y. Xiong, *Angew. Chem. Int. Ed.* **2022**, *61*, e202204225; *Angew. Chem.* **2022**, *134*, e202204225.

[4] a) L. Jiang, A. Gonzalez-Diaz, J. Ling-Chin, A. Malik, A. P. Roskilly, A. J. Smallbone, *Nat. Sustainability* **2020**, *3*, 761–767; b) A. J. J. E. Eerhart, A. P. C. Faaij, M. K. Patel, *Energy Environ. Sci.* **2012**, *5*, 6407–6422.

[5] a) T. Boonyakarn, J. J. Wiesfeld, M. Asakawa, L. Chen, A. Fukuoka, E. J. M. Hensen, K. Nakajima, *ChemSusChem* **2022**, *15*, e202200059; b) C. Ayed, W. Huang, G. Kizilsavas, K. Landfester, K. A. I. Zhang, *ChemPhotoChem* **2020**, *4*, 571–576; c) Y. Lu, C.-L. Dong, Y.-C. Huang, Y. Zou, Z. Liu, Y. Liu, Y. Li, N. He, J. Shi, S. Wang, *Angew. Chem. Int. Ed.* **2020**, *59*, 19215–19221; *Angew. Chem.* **2020**, *132*, 19377–19383.

[6] G. Han, Y.-H. Jin, R. A. Burgess, N. E. Dickenson, X.-M. Cao, Y. Sun, *J. Am. Chem. Soc.* **2017**, *139*, 15584–15587.

[7] a) Z. Zhang, K. Deng, *ACS Catal.* **2015**, *5*, 6529–6544; b) R.-J. van Putten, J. C. van der Waal, E. de Jong, C. B. Rasrendra, H. J. Heeres, J. G. de Vries, *Chem. Rev.* **2013**, *113*, 1499–1597.

[8] a) E. Lam, E. Reisner, *Angew. Chem. Int. Ed.* **2021**, *60*, 23306–23312; *Angew. Chem.* **2021**, *133*, 23494–23500; b) Q.-M. Sun, J.-J. Xu, F.-F. Tao, W. Ye, C. Zhou, J.-H. He, J.-M. Lu, *Angew. Chem. Int. Ed.* **2022**, *61*, e202200872; *Angew. Chem.* **2022**, *134*, e202200872.

[9] B. Zhou, J. Song, Z. Zhang, Z. Jiang, P. Zhang, B. Han, *Green Chem.* **2017**, *19*, 1075–1081.

[10] a) H.-N. Wang, Y.-H. Zou, H.-X. Sun, Y. Chen, S.-L. Li, Y.-Q. Lan, *Coord. Chem. Rev.* **2021**, *438*, 213906; b) A. Meng, L. Zhang, B. Cheng, J. Yu, *Adv. Mater.* **2019**, *31*, 1807660.

[11] J. Low, B. Dai, T. Tong, C. Jiang, J. Yu, *Adv. Mater.* **2019**, *31*, 1802981.

[12] A. R. Jadhav, V. Q. Bui, Y. Cho, Y. Liu, A. Kumar, H. Kim, S. Ajmal, X. Liu, S. Saqlain, J. Lee, H. Kim, Y. D. Kim, S.-G. Kim, H. Lee, *Adv. Energy Mater.* **2022**, *12*, 2102116.

[13] a) J. L. DiMeglio, A. G. Breuhaus-Alvarez, S. Li, B. M. Bartlett, *ACS Catal.* **2019**, *9*, 5732–5741; b) S. Xu, P. Zhou, Z. Zhang, C. Yang, B. Zhang, K. Deng, S. Bottle, H. Zhu, *J. Am. Chem. Soc.* **2017**, *139*, 14775–14782; c) H. Zhang, Q. Wu, C. Guo, Y. Wu, T. Wu, *ACS Sustainable Chem. Eng.* **2017**, *5*, 3517–3523; d) M. Zhang, Z. Li, X. Xin, J. Zhang, Y. Feng, H. Lv, *ACS Catal.* **2020**, *10*, 14793–14800.

[14] a) Y. Chen, Y.-J. Chen, Y. Qi, H.-J. Zhu, X. Huang, Y.-R. Wang, R.-X. Yang, Y.-H. Kan, S.-L. Li, Y.-Q. Lan, *Chem* **2021**, *7*, 463–479; b) Y. Chen, S. Zhang, S. Cao, S. Li, F. Chen, S. Yuan, C. Xu, J. Zhou, X. Feng, X. Ma, B. Wang, *Adv. Mater.* **2017**, *29*, 1606221; c) G. Férey, C. Mellot-Draznieks, C. Serre, F. Millange, J. Dutour, S. Surblé, I. Margiolaki, *Science* **2005**, *309*, 2040–2042; d) H. Li, M. Eddaoudi, M. O'Keeffe, O. M. Yaghi, *Nature* **1999**, *402*, 276–279.

[15] a) H.-Q. Xu, J. Hu, D. Wang, Z. Li, Q. Zhang, Y. Luo, S.-H. Yu, H.-L. Jiang, *J. Am. Chem. Soc.* **2015**, *137*, 13440–13443; b) L. Zhang, P. Cui, H. Yang, J. Chen, F. Xiao, Y. Guo, Y. Liu, W. Zhang, F. Huo, B. Liu, *Adv. Sci.* **2016**, *3*, 1500243; c) M. Zhang, Y. Chen, J.-N. Chang, C. Jiang, W.-X. Ji, L.-Y. Li, M. Lu, L.-Z. Dong, S.-L. Li, Y.-P. Cai, Y.-Q. Lan, *JACS Au* **2021**, *1*, 212–220.

[16] a) T. Devic, C. Serre, *Chem. Soc. Rev.* **2014**, *43*, 6097–6115; b) Y.-J. Liu, W.-H. Fang, L. Zhang, J. Zhang, *Coord. Chem. Rev.* **2020**, *404*, 213099.
[17] a) K. Hong, H. Chun, *Inorg. Chem.* **2013**, *52*, 9705–9707; b) H. L. Nguyen, F. Gándara, H. Furukawa, T. L. H. Doan, K. E. Cordova, O. M. Yaghi, *J. Am. Chem. Soc.* **2016**, *138*, 4330–4333.
[18] a) H. Wei, J. Ning, X. Cao, X. Li, L. Hao, *J. Am. Chem. Soc.* **2018**, *140*, 11618–11622; b) D. A. Cagan, D. Bím, B. Silva, N. P. Kazmierczak, B. J. McNicholas, R. G. Hadt, *J. Am. Chem. Soc.* **2022**, *144*, 6516–6531; c) J.-X. Liu, M.-Y. Gao, W.-H. Fang, L. Zhang, J. Zhang, *Angew. Chem. Int. Ed.* **2016**, *55*, 5160–5165; *Angew. Chem.* **2016**, *128*, 5246–5251.
[19] a) S. Wang, Z. Zhang, H. Zhang, A. G. Rajan, N. Xu, Y. Yang, Y. Zeng, P. Liu, X. Zhang, Q. Mao, Y. He, J. Zhao, B.-G. Li, M. S. Strano, W.-J. Wang, *Matter* **2019**, *1*, 1592–1605; b) Y.-R. Wang, M. Liu, G.-K. Gao, Y.-L. Yang, R.-X. Yang, H.-M. Ding, Y. Chen, S.-L. Li, Y.-Q. Lan, *Angew. Chem. Int. Ed.* **2021**, *60*, 21952–21958; *Angew. Chem.* **2021**, *133*, 22123–22129.
[20] a) C. Guo, M. Liu, G.-K. Gao, X. Tian, J. Zhou, L.-Z. Dong, Q. Li, Y. Chen, S.-L. Li, Y.-Q. Lan, *Angew. Chem. Int. Ed.* **2022**, *61*, e202113315; *Angew. Chem.* **2022**, *134*, e202113315; b) M. Zhang, J.-N. Chang, Y. Chen, M. Lu, T.-Y. Yu, C. Jiang, S.-L. Li, Y.-P. Cai, Y.-Q. Lan, *Adv. Mater.* **2021**, *33*, 2105002; c) B. Luo, Y. Chen, Y. Zhang, J. Huo, *J. Catal.* **2021**, *402*, 52–60.
[21] a) J. Liu, Y. Liu, N. Liu, Y. Han, X. Zhang, H. Huang, Y. Lifshitz, S.-T. Lee, J. Zhong, Z. Kang, *Science* **2015**, *347*, 970–974; b) Z. J. Wang, S. Ghasimi, K. Landfester, K. A. I. Zhang, *Adv. Mater.* **2015**, *27*, 6265–6270.
[22] a) M. Lu, J. Liu, Q. Li, M. Zhang, M. Liu, J.-L. Wang, D.-Q. Yuan, Y.-Q. Lan, *Angew. Chem. Int. Ed.* **2019**, *58*, 12392–12397; *Angew. Chem.* **2019**, *131*, 12522–12527; b) M. Kou, Y. Wang, Y. Xu, L. Ye, Y. Huang, B. Jia, H. Li, J. Ren, Y. Deng, J. Chen, Y. Zhou, K. Lei, L. Wang, W. Liu, H. Huang, T. Ma, *Angew. Chem. Int. Ed.* **2022**, *61*, e202200413; *Angew. Chem.* **2022**, *134*, e202200413.
[23] T. Shi, H. Wang, L. Li, Z. Zhao, C. Wang, X. Zhang, Y. Xie, *Matter* **2022**, *5*, 1004–1015.
[24] L. Liu, M.-Y. Gao, H. Yang, X. Wang, X. Li, A. I. Cooper, *J. Am. Chem. Soc.* **2021**, *143*, 19287–19293.

Manuscript received: June 24, 2022
Accepted manuscript online: July 18, 2022
Version of record online: August 3, 2022